Chinese Chemical Letters 37 (2026) 111176

Contents lists available at ScienceDirect

Chinese Chemical Letters

journal homepage: www.elsevier.com/locate/cclet

Chiral lead-free 0D hybrid metal halides for piezoelectric energy harvesting and underwater ultrasound detection

Hai-Run Yang[a], Chen Zhao[a], Shi-Shuang Huang[a], Zhuo Zhang[a], Xue-Qian Wei[a], Guan-Zhi Wang[a], Tian-Meng Guo[a,b,*], Rui Feng[a,*], Wei Li[a,*], Xian-He Bu[a]

[a] School of Materials Science and Engineering, Nankai University & TKL of Metal and Molecule Based Material Chemistry, Tianjin 300350, China
[b] School of Chemical Engineering and Technology, Hebei University of Technology, Tianjin 300130, China

ARTICLE INFO

Article history:
Received 13 February 2025
Revised 24 March 2025
Accepted 2 April 2025
Available online 3 April 2025

Keywords:
Chiral
Hybrid metal halides
Piezoelectric
Energy harvesting
Ultrasound detection

ABSTRACT

Chiral hybrid metal halides, known for their exceptional piezoelectric properties, facile synthesis, and design flexibility, have become promising candidates for advanced piezoelectric devices. However, most chiral metal halides contain toxic lead and are predominantly restricted to 1D or 2D structures. In contrast, 0D hybrid piezoelectric materials, despite their lower elastic moduli, remain significantly less explored. Here, we report the synthesis of a pair of lead-free chiral 0D hybrid metal halides, *R*-$(APP)_2CoBr_4$ and *S*-$(APP)_2CoBr_4$ (APP = 2-amino-3-phenylpropan-1-ol). First-principles calculations reveal that *S*-$(APP)_2CoBr_4$ exhibits a noticeable shear piezoelectric coefficient while maintaining a relatively low elastic modulus. Furthermore, *S*-$(APP)_2CoBr_4$/PDMS composite films (PDMS = polydimethylsiloxane) were fabricated and their potential for energy harvesting and human motion sensing was investigated. Under a 2 N applied force, a 15 wt% *S*-$(APP)_2CoBr_4$/PDMS composite film exhibits promising performance, generating an open-circuit voltage of 10.21 V and a short-circuit current of 1.02 μA. Additionally, the low acoustic impedance of *S*-$(APP)_2CoBr_4$ (5.80–6.67 MRayl) and its compatibility with water (1.5 MRayl) facilitate efficient ultrasound transmission in composite devices, ensuring precise localization of ultrasound sources. These findings offer valuable insights into the potential of lead-free 0D hybrid metal halides for advanced electromechanical applications.

© 2026 Published by Elsevier B.V. on behalf of Chinese Chemical Society and Institute of Materia Medica, Chinese Academy of Medical Sciences.

Piezoelectric materials with non-centrosymmetric structures generate polarization charges under mechanical stress, enabling their use in actuators, ultrasonic transducers, and sensors [1–3]. Materials exhibiting large longitudinal piezoelectric strain coefficients (d_{33}) dominate most commercial applications, such as $BaTiO_3$ and $PbZr_xTi_{1-x}O_3$ ($0 < x < 1$) [4,5]. However, the complex fabrication processes and environmental concerns of traditional piezoelectric materials have limited their broader application. Moreover, the growing demand for flexible and wearable devices has driven significant advancements in the development of flexible piezoelectric materials [6], such as polyvinylidene fluoride (PVDF) [7–9]. Despite their advantages, such copolymers have faced persistent challenges, including fabrication difficulties, high costs, and poor thermal stability [10]. Recently, hybrid metal halides have garnered considerable attention for their chemical versatility and structural diversity [11–18]. These materials provide new opportunities for molecular engineering and the design of piezoelectric materials with multi-dimensional properties. For instance, among one-dimensional (1D) piezoelectric materials, $(TMFM)_x(TMCM)_{1-x}$-$CdCl_3$ (TMFM = trimethylfluoromethyl ammonium, TMCM = trimethylchloromethyl ammonium) exhibited a large d_{33} of 1540 pC/N [19], while in two-dimensional (2D) piezoelectric materials, $(ATHP)_2PbBr_4$ (ATHP = 4-aminotetrahy-dropyran) showed a piezoelectric voltage constant (g_{33}) of 660.3×10^{-3} V m/N [20], which was twice that of PVDF ($g_{33} = 286.7 \times 10^{-3}$ V m/N). These low dimensional materials demonstrate considerable potential as effective alternatives to traditional piezoelectric materials. However, the piezoelectric properties of hybrid metal halide crystals are significantly influenced by the spatial structure and electronic effects of the organic ligands, as well as their interactions with the inorganic framework. Furthermore, when the ligands are chiral organic molecules, their inherent asymmetry induces circularly polarized luminescence [21,22] and nonlinear optical behavior [23,24], while also driving a structural transition from symmetry to asymmetry [25,26], thereby enabling piezoelectricity.

Hybrid metal halides have demonstrated significant potential in human sensing [27] and energy harvesting applications [28–30],

* Corresponding authors.
E-mail addresses: guotianmeng@hebut.edu.cn (T.-M. Guo), fengrui@nankai.edu.cn (R. Feng), wl276@nankai.edu.cn (W. Li).

https://doi.org/10.1016/j.cclet.2025.111176
1001-8417/© 2026 Published by Elsevier B.V. on behalf of Chinese Chemical Society and Institute of Materia Medica, Chinese Academy of Medical Sciences.

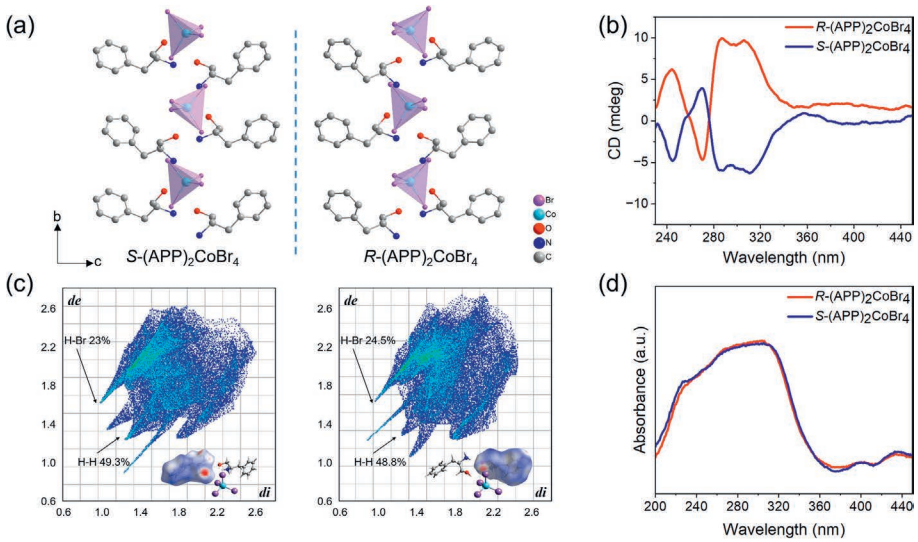


Fig. 1. (a) Crystal structures of *R*-$(APP)_2CoBr_4$ (right) and *S*-$(APP)_2CoBr_4$ (left) along the *a*-axis. Note that the extra hydrogen atoms are omitted for clarity. (b) CD signals of *R*/*S*-$(APP)_2CoBr_4$. (c) The 2D fingerprints of *S*-$(APP)_2CoBr_4$. The inserts are the Hirshfeld surfaces of the organic cations. (d) UV-visible absorption spectra of *R*-$(APP)_2CoBr_4$ and *S*-$(APP)_2CoBr_4$.

but their use in underwater ultrasound detection remains largely underexplored. While inorganic piezoelectric ceramics exhibit excellent piezoelectric properties, their high-density results in elevated acoustic impedance, limiting efficient sound wave transmission and restricting their applicability in ultrasound detection [31]. In contrast, metal halides are highly sensitive to mechanical deformations, acoustic impedances closely aligned with water [32], and low elastic moduli, making them suitable for underwater ultrasound detection applications [33].

In this study, two non-centrosymmetric 0D lead-free hybrid metal halides, *R*-$(APP)_2CoBr_4$ and *S*-$(APP)_2CoBr_4$, were synthesized. *S*-$(APP)_2CoBr_4$ displays three distinct shear piezoelectric coefficients, and the *S*-$(APP)_2CoBr_4$/PDMS composite film exhibits outstanding performance in energy harvesting and human motion sensing. First-principles calculations reveal that *S*-$(APP)_2CoBr_4$ possesses a low elastic modulus and an acoustic impedance similar to water. Consequently, the *S*-$(APP)_2CoBr_4$ composite film device displays exceptional sensitivity for underwater ultrasound detection.

R-$(APP)_2CoBr_4$ and *S*-$(APP)_2CoBr_4$ both crystallize in the chiral space group $P2_12_12_1$, with cell parameters of $a = 8.3888(2)/8.38400(10)$ Å, $b = 12.3331(3)/12.33880(10)$ Å, $c = 23.6667(5)/23.66890(10)$ Å, respectively. As shown in Fig. 1a, both *R*-$(APP)_2CoBr_4$ (right) and *S*-$(APP)_2CoBr_4$ (left) exhibit a characteristic 0D packing structure. Each asymmetric unit comprises one $[CoBr_4]^{2-}$ tetrahedron and two crystallographically independent organic amine cations for charge balance. Each Co^{2+} ion is coordinated by four Br^- anions to form a $[CoBr_4]^{2-}$ tetrahedron, with the $[CoBr_4]^{2-}$ tetrahedra interacting with surrounding $[APP]^+$ cations *via* electrostatic forces.

The chirality of *R*/*S*-$(APP)_2CoBr_4$ crystals was confirmed through circular dichroism (CD) spectroscopy of a crystal powder/KBr pellet measured in the 250–600 nm range (Fig. 1b). Distinct, opposite CD signals observed in the 230–450 nm range, demonstrating the successful transfer of chirality from the organic amine to the crystal structure, as indicated by the Cotton effect. The UV–visible absorption spectra in Fig. 1d display identical characteristic absorptions for both crystals in the 230–450 nm range, consistent with the CD spectroscopy signals [34].

Hirshfeld surface analysis and corresponding 2D fingerprint plots were used to investigate the intermolecular interactions between organic cations and the inorganic tetrahedra in *R*/*S*-$(APP)_2CoBr_4$. The Hirshfeld surface color variations (red, white, blue) represent interatomic distances shorter, equal to, and longer than the van der Waals distances, respectively [35,36]. In Fig. 1c, the prominent red regions near the -OH groups on the Hirshfeld surfaces of *S*-$(APP)_2CoBr_4$ indicate strong intermolecular interactions between the organic cations and the inorganic tetrahedra. However, variations in interatomic distances cause differences in the red area size on the surface of *S*-$(APP)^+$, reflecting differing H-Br proportions. Similarly, the Hirshfeld surfaces of *R*-$(APP)_2CoBr_4$ (Fig. S1 in Supporting information) show comparable differences. In the 2D fingerprint plots, d_i and d_e represent distances from the organic cations to surrounding atoms inside and outside the Hirshfeld surface, respectively. A prominent feature in both crystal structures is the sharp peak in the bottom-left corner of the 2D fingerprint plots, indicating the organic cations act as strong hydrogen bond donors ($d_i < d_e$). The small sum of $d_i + d_e$ further confirms strong hydrogen bonding between the tetrahedra and the organic cations. These results indicate strong interactions between the organic cations and the inorganic chains, explaining the materials' stability and decomposition resistance up to 230 °C, as confirmed by thermogravimetric analysis (Fig. S2 in Supporting information). Differential scanning calorimetry (DSC) measurements (Fig. S3 in Supporting information) reveal reversible melting and crystallization behavior in *R*/*S*-$(APP)_2CoBr_4$, demonstrating its processability. Phase purity was confirmed by powder X-ray diffraction (PXRD, Fig. S4 in Supporting information), where experimental diffraction peaks closely matched the simulated pattern, indicating high crystallinity. Raman and infrared spectroscopy (Fig. S5 in Supporting information) further verified the enantiomeric crystal structures with consistent results.

The elastic properties of *R*/*S*-$(APP)_2CoBr_4$ are crucial for understanding their mechanical performance and intrinsic piezoelectric behavior under practical applications [37–39]. In general, 0D materials exhibit a lower elastic modulus compared to their higher-dimensional counterparts, as summarized in Table S2 (Supporting information). The elastic stiffness constants (C_{ij}) of *S*-$(APP)_2CoBr_4$, determined *via* first-principles calculations, are listed in Table S3 (Supporting information). Based on the elastic stiffness coefficients (C_{ij}), Young's modulus (E) and shear modulus (G) were calculated, and their 3D representations are depicted in Figs. 2a and b, respectively. The maximum and minimum values of Young's modu-

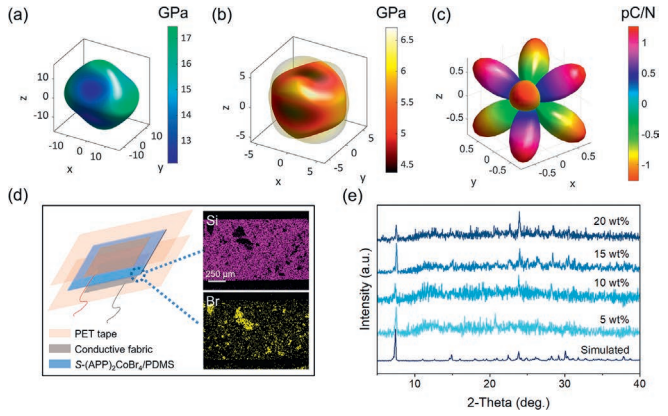


Fig. 2. 3D representations of (a) Young's moduli, (b) shear moduli, and (c) piezoelectric constants of *S*-$(APP)_2CoBr_4$. (d) Schematic diagram of the device structure and cross-sectional EDS-mapping images of the 15 wt% *S*-$(APP)_2CoBr_4$/PDMS composite film. (e) The PXRD patterns of the *S*-$(APP)_2CoBr_4$/PDMS films with different contents.

lus, along with their corresponding directions, are shown in Fig. S6 (Supporting information). The maximum Young's modulus (E_{max}) of *S*-$(APP)_2CoBr_4$ is 17.48 GPa along the <001> direction, while the minimum (E_{min}) is 12.13 GPa along <011>. This variation is attributed to differences in the crystal structure and packing density, as illustrated in Fig. S7 (Supporting information). The more compact arrangement of $[CoBr_4]^{2-}$ tetrahedra along <001> increases Young's modulus. In contrast, the relatively less dense packing along the <011> direction reduces the modulus.

Similarly, the shear modulus (G) exhibits anisotropy, with $G_{max} = 6.703$ GPa along the $(10\bar{1})$ <101> direction (Fig. S8a in Supporting information) and $G_{min} = 4.38$ GPa along the (010) <001> direction (Fig. S8b in Supporting information), resulting in an anisotropy ratio of $G_{max}/G_{min} = 1.53$. Fig. S8b (Supporting information) reveals that the $[CoBr_4]^{2-}$ tetrahedra and *S*-$(APP)^+$ are packed in a layer-like fashion along the <001>, facilitating easier shearing on the (010) plane. In contrast, as shown in Fig. S9 (Supporting information), the interwoven structure of $[CoBr_4]^{2-}$ tetrahedra and *S*-$(APP)^+$ cations along <101> increases resistance to shear stress on the $(10\bar{1})$ plane. The Poisson's ratio (ν) demonstrated in Fig. S10 (Supporting information) ranges from maximum (0.42) to minimum (0.23), highlighting the materials' excellent elastic deformation capacity along specific directions.

The piezoelectric strain coefficients matrix of *S*-$(APP)_2CoBr_4$ was calculated using $[d] = [e][s]$, where $[e]$ and $[s]$ are the piezoelectric stress and elastic compliance constants [40]. As a member of the orthorhombic 222-point group, *S*-$(APP)_2CoBr_4$ exhibits shear piezoelectric coefficients d_{14}, d_{25}, and d_{36}. Fig. 2c and Fig. S11 (Supporting information) present 3D and 2D visualizations of these constants with specific values of d_{ij} (unit of pC/N) matrix detailed in Table S4 (Supporting information). Notably, the shear piezoelectric coefficient $d_{25} = -4.92$ pC/N reflects a strong shear response, attributed to the low packing density in the (010) plane, which facilitates shear deformation and enhances the piezoelectric effect.

R/*S*-$(APP)_2CoBr_4$, with their soft nature and favorable piezoelectric properties, are promising candidates for sensors and piezoelectric energy harvesting applications. However, powder-based devices face performance challenges, including triboelectric effects and charge cancellation from direct crystallite contact [41]. To enhance performance, *S*-$(APP)_2CoBr_4$/PDMS composite films were fabricated with varying weight ratios (wt%) of crystal powder (5 %, 10 %, 15 %, and 20 %). Scanning electron microscopy (SEM) and elemental mapping (Fig. 2d and Fig. S12 in Supporting information) show a uniform cross-sectional morphology, with evenly dispersed Br elements in the PDMS matrix. Increased content of *S*-$(APP)_2CoBr_4$ powder results in more widespread Br elements in the PDMS matrix. However, when the powder content reaches 20 wt%, Br elements tend to aggregate, likely due to the agglomeration of piezoelectric particles [42]. The composite films demonstrate excellent mechanical properties, with Young's moduli ranging from 1.83 MPa to 2.38 MPa, as shown by the stress-strain curves in Fig. S13 (Supporting information). A lower modulus promotes energy harvesting by allowing greater strain under the same stress [43]. The PXRD patterns of films with different compositions (Fig. 2e) confirm the retention of the crystal structure, with prominent peaks at 7.46° (002), 23.67° (025), and 28.42° (205). Increased content introduces new diffraction peaks, indicating a progressive enhancement in crystallinity.

Dielectric properties are vital for assessing the performance of piezoelectric energy harvesters [44,45]. Capacitance (C), impedance (Z), relative permittivity (ε_r), and Q-factor (Q) of the 15 wt% composite film were systematically measured, which are presented in Figs. S14 and S15 (Supporting information). In the low-frequency range (1 kHz to 100 kHz), capacitance decreases rapidly, but stabilizes at higher frequencies due to the lag of the material's polarization behind the external electric field. Despite the decline in capacitance, impedance does not necessarily increase, as high-frequency polarization limitations result in nonlinear charge responses [46]. At higher frequencies, increased dielectric losses reduce overall impedance. As frequency rises from 1 kHz to 10 MHz, the ε_r of the composite film decreases. In the low-frequency region, ε_r remains high due to enhanced polarization response to the external electric field, while at higher frequencies, electronic polarization dominates, leading to a significant reduction in ε_r. Despite this, the composite film exhibits a much lower ε_r compared to conventional perovskite ceramics. Based on $g = d/\varepsilon_r$ (where g is the piezoelectric voltage constant and d is the piezoelectric constant), the high g value suggests excellent electromechanical efficiency. Consequently, *S*-$(APP)_2CoBr_4$/PDMS composite films show strong potential for high-performance sensor applications. Moreover, the Q of the *S*-$(APP)_2CoBr_4$ - based piezoelectric energy harvester exceeds 75, further supporting its suitability for sensor-based technologies.

The exceptional piezoelectric properties of *R*/*S*-$(APP)_2CoBr_4$ highlight their potential for applications in energy harvesting and sensing technologies. To demonstrate functionality, *S*-$(APP)_2CoBr_4$/PDMS composite films (2×2 cm^2) were sandwiched between conductive fabric electrodes, encapsulated with polyethylene terephthalate (PET) tape, forming a simple piezoelectric device (Fig. S16 in Supporting information). The device was tested using a custom test system that applied periodic mechanical tapping at 10 Hz. Under the 2 N force, charge separation within the *S*-$(APP)_2CoBr_4$ crystals was induced by the misalignment of positive and negative charge centers, generating a piezoelectric response through the shear effect. As shown in Fig. 3a, the open-circuit voltage (V_{oc}) increased with composite concentration, rising from 1.79 V (5 wt%) to 10.21 V (15 wt%), outperforming chiral molecular crystals and chiral lead halide perovskites (Table S5 in Supporting information). However, further increasing the concentration to 20 wt% reduced V_{oc} to 1.75 V, attributed to excessive particle aggregation, which elevated the dielectric constant and induced Maxwell-Wagner-Sillars polarization [47], as corroborated by SEM and elemental mapping images. A similar trend was observed for short-circuit current (I_{sc}), where the 15 wt% composite achieved the highest I_{sc} of 1.02 μA (Fig. 3d).

The 15 wt% composite film was selected for further piezoelectric testing on its optimal performance. To verify the piezoelectric effect, V_{oc} (Fig. 3b) and I_{sc} (Fig. 3e) were measured with electrodes connected in forward and reverse configurations. V_{oc} exhibited positive values in the forward connection and negative values in the reverse, confirming the piezoelectric origin of the signals and excluding triboelectric contributions [48]. Measurements on

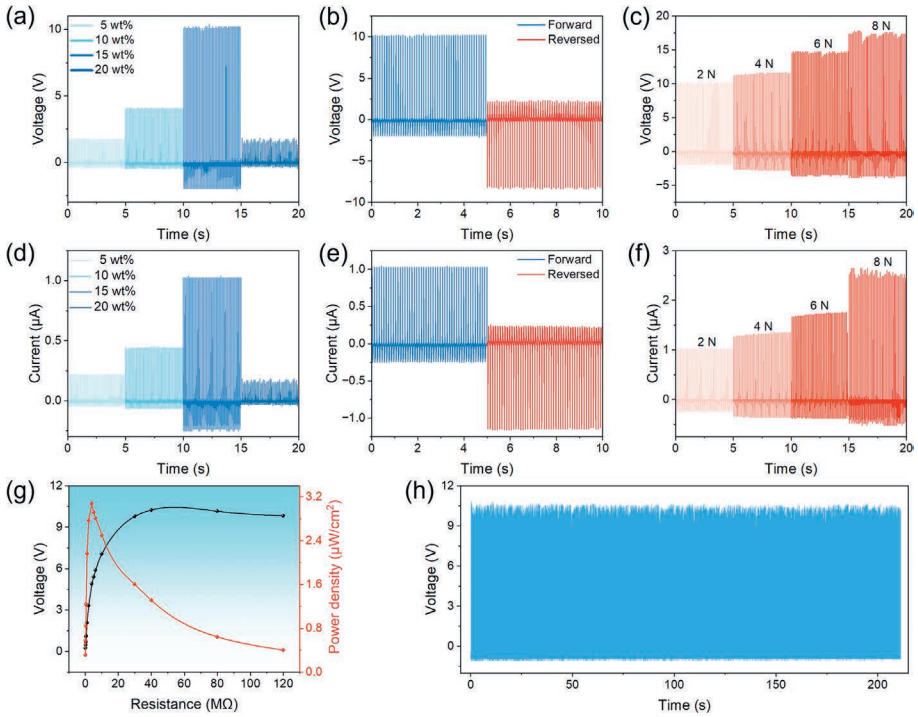


Fig. 3. (a) V_{oc} and (d) I_{sc} of composite films with different contents of *S*-$(APP)_2CoBr_4$. (b) V_{oc} and (e) I_{sc} output of the 15 % *S*-$(APP)_2CoBr_4$/PDMS film when reversing the electrodes. The applying force-dependent (c) V_{oc} and (f) I_{sc} performances with the 15 % *S*-$(APP)_2CoBr_4$/PDMS film. (g) The resistance-dependent voltages and power densities. (h) Cyclic performance of the 15 % *S*-$(APP)_2CoBr_4$/PDMS film over 2000 cycles.

pure PDMS film (Fig. S17 in Supporting information) showed no reverse signal, further ruling out triboelectric effects. Further, output signals were collected under varying applied forces (2, 4, 6, and 8 N), as shown in Figs. 3c and f. V_{oc} increased from 10.21 V to 17.58 V, while I_{sc} rose from 1.02 μA to 2.61 μA. Additionally, output voltage increased with frequency (Fig. S18 in Supporting information), as higher frequencies generate more charge per unit time, enhancing electric displacement and V_{oc}. The electric power characteristics of the 15 wt% composite film were further investigated under varying external load resistances (1–120 MΩ, Fig. 3 g). A peak power density of 3.07 μW/cm^2 was achieved at 3.9 MΩ, comparable to other hybrid piezoelectric/PDMS composites (Table S5 in Supporting information). Mechanical and temporal stability was assessed by applying a continuous 2 N force at 10 Hz for 200 s, with V_{oc} remaining stable over 2000 cycles (Fig. 3h).

The piezoelectric energy harvester was tested as a sensor for monitoring various human motions. Subtle elbow flexion (Fig. S19a in Supporting information) produced a stable 0.2 V output. When positioned under a shoe to detect forces generated by foot tapping (Fig. S19b in Supporting information), the piezoelectric response showed distinct peaks, demonstrating high sensitivity to dynamic force variations. Its flexibility also allowed attachment to a knuckle for monitoring finger bending, where flexion generated a positive voltage and release produced a negative signal. As shown in Fig. S19c (Supporting information), the output voltage increased proportionally with the degree of bending, correlating with greater applied stress. These results highlight the potential of *S*-$(APP)_2CoBr_4$/PDMS films for precise motion detection in wearable applications.

The piezoelectric energy harvester demonstrates exceptional potential for underwater ultrasound detection due to its high electro-mechanical energy conversion efficiency. The schematic diagram of the self-developed underwater ultrasound detection device is illustrated in Fig. 4a. Ultrasound probes with center frequencies of 2.5, 5.0, and 10.0 MHz were used for testing. As depicted in Fig. 4b, the output voltages for the 5 MHz probe exhibit a clear distance dependence, with peak-to-peak voltages ($V_{p\text{-}p}$) of 440.1, 250.8, and 103.7 mV at probe distances of 7.5, 10.5, and 13.5 mm, respectively, consistent with decreased signal amplitude at greater distances. Similar trends were observed for the 2.5 MHz and 10 MHz probes (Figs. S20 and S21 in Supporting information). The resulting characteristic frequencies of 2.63, 4.34, and 11.11 MHz (Figs. 4c–e) closely match the probe center frequencies, confirming the accurate capture of ultrasound frequency information. To assess the long-term reliability of the composite film device, cyclic immersion testing was performed over 36 h at room temperature using a 2.5 MHz ultrasonic probe, with results detailed in Fig. S22 (Supporting Information). The results demonstrate that the encapsulated device exhibited excellent stability. First-principles calculations determined the sound velocity (c) in the *S*-$(APP)_2CoBr_4$ crystal to range from 3.13 km/s to 3.60 km/s. Accordingly, the corresponding acoustic impedance z was computed using the relation $z = \rho \cdot c$, where ρ is the material density [49], resulting in values between 5.80–6.67 MRayl. Notably, the acoustic impedance of water (1.50 MRayl) and the PDMS matrix (1.62 MRayl) [50] are closely matched, ensuring efficient ultrasonic transmission without the need for an intermediate coupling layer. This eliminates energy dissipation and excessive reflection, a common requirement for oxide-based devices.

In summary, 0D hybrid lead-free metal halides *R*-$(APP)_2CoBr_4$ and *S*-$(APP)_2CoBr_4$ were successfully synthesized and characterized, exhibiting exceptional piezoelectric properties. First-principles calculations revealed that *S*-$(APP)_2CoBr_4$ has low elastic moduli and excellent piezoelectric characteristics, making it a strong candidate for energy harvesting applications. Flexible *S*-$(APP)_2CoBr_4$/PDMS composite films were fabricated and achieved a maximum V_{oc} of 10.21 V, I_{sc} of 1.02 μA, with a power density of 3.07 μW/cm^2 under a 2 N force, demonstrating high potential for precise human motion sensing. Additionally, the low acoustic impedance of *S*-$(APP)_2CoBr_4$ (5.80 MRayl) matches that of water,

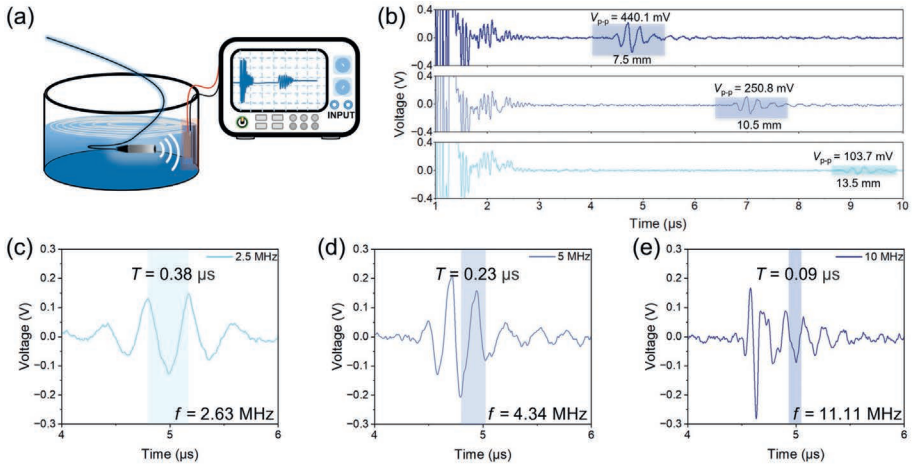


Fig. 4. Ultrasound detection using the 15 wt% *S*-$(APP)_2CoBr_4$/PDMS film. (a) Schematic diagram of the experimental setup for underwater ultrasound detection. (b) Output voltage based on different distances between the 5 MHz probe and the composite film. Characteristic signals recorded by the composite film when using probes with frequencies of (c) 2.5 MHz, (d) 5 MHz and (e) 10 MHz.

enabling efficient energy transmission without a coupling layer. The films effectively distinguish ultrasound frequencies and detect source distances through characteristic signal responses. This study broadens the application scope of 0D hybrid metal halides in sensing and ultrasound detection technologies.

Declaration of competing interest

The authors declare that they have no known competing financial interests or personal relationships that could have appeared to influence the work reported in this paper.

CRediT authorship contribution statement

Hai-Run Yang: Writing – original draft. **Chen Zhao:** Data curation. **Shi-Shuang Huang:** Investigation. **Zhuo Zhang:** Software. **Xue-Qian Wei:** Formal analysis. **Guan-Zhi Wang:** Formal analysis. **Tian-Meng Guo:** Validation, Supervision. **Rui Feng:** Writing – review & editing, Supervision. **Wei Li:** Writing – review & editing, Supervision, Resources, Conceptualization. **Xian-He Bu:** Supervision, Resources, Conceptualization.

Acknowledgments

The authors acknowledge the financial support from the National Key Research and Development Program of China (No. 2022YFA1503300) and the National Natural Science Foundation of China (No. 22375105).

Supplementary materials

Supplementary material associated with this article can be found, in the online version, at doi:10.1016/j.cclet.2025.111176.

References

[1] M. Waqar, H. Wu, J. Chen, K. Yao, J. Wang, Adv. Mater. 34 (2022) 2106845.
[2] A. Petritz, E. Karner-Petritz, T. Uemura, et al., Nat. Commun. 12 (2021) 2399.
[3] A.M. Manjón-Sanz, M.R. Dolgos, Chem. Mater. 30 (2018) 8718–8726.
[4] J. Li, W. Qu, J. Daniels, et al., Science 380 (2023) 87–93.
[5] H.F. Ni, J.H. Lin, G. Teri, et al., Chin. Chem. Lett. 36 (2025) 109690.
[6] F. Lang, J. Pang, X.H. Bu, eScience 4 (2024) 100231.
[7] Q.Q. Jia, J.Q. Luo, Z.Y. Xue, et al., Chin. Chem. Lett. 36 (2025) 110471.
[8] H. Kawai, Jpn. J. Appl. Phys. 8 (1969) 975.
[9] Z.X. Huang, L.W. Li, Y.Z. Huang, et al., Nat. Commun. 15 (2024) 819.
[10] M.R.B. Domalanta, S. Ferdousi, E.G.D. Armas, Y. Jiang, E.B. Caldona, Chem. Eng. J. 493 (2024) 152616.
[11] J. Men, K. Xu, T. Sha, et al., Chin. Chem. Lett. 35 (2024) 108427.
[12] C. Zhao, Z.Y. Li, Y.J. Gong, et al., Chem. Asian J. 20 (2025) e202401506.
[13] Y.M. You, W.Q. Liao, D. Zhao, et al., Science 348 (2017) 306–309.
[14] H.P. Lv, W.Q. Liao, Y.M. You, R.G. Xiong, J. Am. Chem. Soc. 144 (2022) 22325–22331.
[15] Y.Y. Zhang, J.Q. Luo, Y. Han, et al., Chin. Chem. Lett. 36 (2025) 109530.
[16] J.Q. Zhao, D.Y. Wang, T.Y. Yan, et al., Angew. Chem. Int. Ed. 63 (2024) e202412350.
[17] F. Nie, D. Yan, Nat. Commun. 15 (2024) 5519.
[18] C. Xing, B. Zhou, D. Yan, W.H. Fang, CCS Chem. 5 (2023) 2866–2876.
[19] W.Q. Liao, D. Zhao, Y.Y. Tang, et al., Science 363 (2019) 1206–1210.
[20] X.G. Chen, X.J. Song, Z.X. Zhang, et al., J. Am. Chem. Soc. 142 (2020) 1077–1082.
[21] J.T. Lin, D.G. Chen, L.S. Yang, et al., Angew. Chem. Int. Ed. 60 (2021) 21434–21440.
[22] Y. Deng, F. Li, Z. Zhou, et al., Chin. Chem. Lett. 35 (2024) 109085.
[23] M. Yang, H. Cheng, Y. Xu, M. Li, Y. Ai, Chin. Chem. Lett. 33 (2022) 2143–2146.
[24] D. Fu, J. Xin, Y. He, et al., Angew. Chem. Int. Ed. 60 (2021) 20021–20026.
[25] R.W. Whatmore, Y.M. You, R.G. Xiong, C.B. Eom, APL Mater. 9 (2021) 070401.
[26] D.F. Caffrey, T. Gorai, B. Rawson, et al., Adv. Sci. 11 (2024) 2303448.
[27] L.C. An, C. Zhao, Y. Zhao, et al., Small Struct. 4 (2023) 2300135.
[28] X. Ju, J. Kong, G. Qi, et al., eScience 4 (2024) 100223.
[29] L.J. Ji, C. Zhao, T.Y. Yang, et al., APL Mater. 12 (2024) 091116.
[30] Y.J. Gong, L.C. An, Y. Zhang, et al., Adv. Funct. Mater. 34 (2024) 2402649.
[31] H.Y. Zhang, Chem. Sci. 13 (2022) 5006–5013.
[32] T.M. Guo, F.F. Gao, Z.G. Li, et al., APL Mater. 8 (2020) 101106.
[33] T.M. Guo, F.F. Gao, Y.J. Gong, et al., J. Am. Chem. Soc. 145 (2023) 22475–22482.
[34] R.G. Xiong, S.Q. Lu, Z.X. Zhang, et al., Angew. Chem. Int. Ed. 59 (2020) 9574–9578.
[35] P.R. Spackman, M.J. Turner, J.J. McKinnon, et al., J. Appl. Crystallogr. 54 (2021) 1006–1011.
[36] M.A. Spackman, J.J. McKinnon, CrystEngComm 4 (2002) 378–392.
[37] Z.X. Wang, H. Zhang, F. Wang, et al., J. Am. Chem. Soc. 142 (2020) 12857–12864.
[38] K. Li, Y. Qin, Z.G. Li, et al., Coord. Chem. Rev. 470 (2022) 214692.
[39] H. Wang, H. Liu, Z. Zhang, et al., npj Comput. Mater. 5 (2019) 17.
[40] T.M. Guo, Y.J. Gong, Z.G. Li, et al., Small 18 (2022) 2103829.
[41] T. Yang, D. Jia, B. Xu, et al., eScience 4 (2024) 100273.
[42] H. Chen, L. Zhou, Z. Fang, et al., Adv. Funct. Mater. 31 (2021) 2011073.
[43] J. Li, Z. Zhu, L. Fang, et al., Nanoscale 9 (2017) 14215–14228.
[44] V. Jella, S. Ippili, J.H. Eom, et al., Nano Energy 57 (2019) 74–93.
[45] Y.J. Gong, Z.G. Li, H. Chen, et al., Matter 6 (2023) 2066–2080.
[46] E.E. Morgan, A. Zohar, S. Lipkin, et al., Chem. Mater. 36 (2024) 1228–1237.
[47] Y. Sun, Y. Lu, X. Li, et al., J. Mater. Chem. A 8 (2020) 12003–12012.
[48] A.A. Khan, G. Huang, M.M. Rana, et al., Nano Energy 86 (2021) 106039.
[49] Z.G. Li, K. Li, L.Y. Dong, et al., Research 2021 (2021) 9850151.
[50] C. Sukkasem, S. Sasivimolkul, P. Suvarnaphaet, S. Pechprasarn, J. Curr. Sci. Technol. 11 (2021) 197–207.